DYNAMO-GENERATED TURBULENCE AND LARGE-SCALE MAGNETIC FIELDS IN A KEPLERIAN SHEAR FLOW

AXEL BRANDENBURG[1]

Advanced Study Program and High Altitude Observatory, National Center for Atmospheric Research,[2] P.O. Box 3000, Boulder, CO 80307-3000

ÅKE NORDLUND

Theoretical Astrophysics Center, Blegdamsvej 17, DK-2100 Copenhagen Ø, Denmark; and Copenhagen University Observatory

ROBERT F. STEIN

Department of Physics and Astronomy, Michigan State University, East Lansing, MI 48824

AND

ULF TORKELSSON

Lund Observatory, Box 43, S-221 00 Lund, Sweden; and Sterrenkundig Instituut, Utrecht

ABSTRACT

The nonlinear evolution of magnetized Keplerian shear flows is simulated in a local, three-dimensional model, including the effects of compressibility and stratification. Supersonic flows are initially generated by the Balbus-Hawley magnetic shear instability. The resulting flows regenerate a turbulent magnetic field which, in turn, reinforces the turbulence. Thus, the system acts like a dynamo that generates its own turbulence. However, unlike usual dynamos, the magnetic energy exceeds the kinetic energy of the turbulence by a factor of 3–10. By assuming the field to be vertical on the outer (upper and lower) surfaces we do not constrain the horizontal magnetic flux. Indeed, a large-scale toroidal magnetic field is generated, mostly in the form of toroidal flux tubes with lengths comparable to the toroidal extent of the box. This large-scale field is mainly of even (i.e., quadrupolar) parity with respect to the midplane and changes direction on a timescale of ~ 30 orbits, in a possibly cyclic manner. The effective Shakura-Sunyaev alpha viscosity parameter is between 0.001 and 0.005, and the contribution from the Maxwell stress is ~ 3–7 times larger than the contribution from the Reynolds stress.

Subject headings: accretion: accretion disks — MHD — shock waves — turbulence

1. INTRODUCTION

The origin of turbulence in accretion disks is unclear. There are strong arguments that magnetic fields may be important for causing the onset of turbulence (Balbus & Hawley 1991; Kaisig, Tajima, & Lovelace 1992; Kumar, Coleman, & Kley 1994; Zhang, Diamond, & Vishniac 1994; Goodman & Xu 1994). On the other hand, if the turbulence in the disk is of nonmagnetic origin, it ought to be a nonlinear instability (e.g., Dubrulle & Knobloch 1992; Dubrulle 1993), because locally Keplerian shear flows are linearly stable (Stewart 1975). Non-linear instabilities in Couette and Poiseuille flows have previously been investigated (e.g., Zahn et al. 1974; Orszag & Kells 1980; Dubrulle & Zahn 1991), but such flows are forced by the boundaries and therefore hardly applicable to accretion disks (except perhaps near the inner boundary of the disk). There are numerous simulations of turbulence in homogeneous shear flows (e.g., Rogers & Moin 1987; Rogers 1991), but in those cases rotation is not present. Cabot & Pollack (1992) performed simulations of shear flows in the presence of rotation and variable gravity, but here the turbulence is driven by thermal convection. Although convection is thought to be important in protoplanetary disks, where the opacity is high (e.g., Kley, Papaloizou, & Lin 1993), the heating results only from turbulent viscosity which, in turn, requires the existence of turbulence. The turbulence may be weak, especially when most of the angular momentum is transported by the Maxwell stress (e.g., Pudritz 1981; Campbell 1992), but even then we are faced with the problem of explaining this weak turbulence. Other potentially important mechanisms for driving an instability in accretion disks are: tidally excited spiral waves (Różyczka & Spruit 1993; Morfill, Spruit, & Levy 1993), inertial waves (Vishniac, Jin, & Diamond 1990; Vishniac 1993), global, nonaxisymmetric instabilities, in particular for thick disks (e.g., Papaloizou & Pringle 1984), and tidal forces which drive small-scale turbulence (Ryu & Goodman 1992, 1994). The effects of radiation drag on the accretion disk have been discussed (e.g., Miller & Lamb 1993; Walker 1992), but this is of importance only for accretion onto black holes and neutron stars.

A natural source of turbulence may be a *linear* magneto-hydrodynamic instability (Balbus & Hawley 1991). This instability is local in that it exists even if the global disk structure is ignored, but it is modified when global effects are taken into account (Curry, Pudritz, & Sutherland 1994). This instability has been known for more than three decades (Velikhov 1959; Chandrasekhar 1960, 1961), but its importance for accretion disks was first pointed out by Balbus & Hawley (1991), and it is therefore often referred to as the Balbus-Hawley instability. The instability requires a magnetic field that can be generated either outside the disk (e.g., in the central object) or in the disk itself. Here we consider the latter possibility where the motions resulting from the instability act as a dynamo to sustain the magnetic field.

In a recent paper, Hawley, Gammie, & Balbus (1995) have studied the Balbus-Hawley instability in the presence of an irregular magnetic field and have shown that this field can sustain self-excited turbulence. In their model there is no vertical gravity, and therefore the Parker instability (Parker 1979) does not operate. This is in contrast to the dynamo model of Tout & Pringle (1992), which invokes the Parker instability to transform an azimuthal magnetic field into a vertical field. Meanwhile, Stone & Hawley (1995) included vertical gravity with substantial density stratification and found qualitatively similar results as Hawley et al. (1995). They also showed that the saturated state is essentially independent of the initial magnetic field geometry.

The purpose of the present paper is twofold. First of all, simulating dynamo action which generates its own turbulence is a formidable problem in dynamo theory and is central to the understanding of accretion disks which would not exist if there was no enhanced (e.g., turbulent) angular momentum transport. The papers by Stone & Hawley (1995) and Hawley et al. (1995) are based on the same algorithm, and it is desirable to verify their results using an independent method. Second, in the simulations of Stone & Hawley (1995) the total magnetic flux through the box was conserved and zero for all times, because periodic boundary conditions were used. In the present paper we assume that the magnetic field at the upper and lower surfaces is vertical, but that the magnetic fieldlines can move freely across the surface.

A vertical field boundary condition is often used in magneto-convection simulations (e.g., Hurlburt & Toomre 1988). This condition simulates the tendency of magnetic buoyancy to turn a horizontal magnetic field vertical. We assume periodic (or quasi-periodic) boundary conditions in the horizontal directions (see below), which implies that the flux through the upper and lower surfaces is conserved (see § 2.2 below). In order to have a well-posed dynamo problem, the field must be able to decay freely, and therefore we require the vertical flux to be zero initially (and thus for all times). Unlike periodic or perfectly conducting upper and lower surfaces, the vertical field condition does not constrain the magnetic flux in the two horizontal directions. We do indeed find generation of a net magnetic field. This is easily seen in the dominant toroidal component, which shows signs of cyclic reversals on a time-scale of ~20–30 orbits.

We should point out that the turbulence is transonic and temporarily even supersonic. It is therefore necessary to include shock capturing viscosities. It should also be emphasized that no dynamo alpha effect (e.g., Krause & Rädler 1980) is imposed; that is, the regeneration of magnetic fields is due solely to the interaction between the turbulence and the magnetic field at the resolved scales, and that even the turbulence is a result of such an interaction.

2. THE MODEL

2.1. *Basic Equations*

We consider a local Cartesian frame of reference in the disk, where x, y, and z correspond to the radial, torodial, and vertical directions, respectively. We rewrite the equations such that there is no systematic variation of the variables along the x-direction. This is achieved by solving only for the deviations $\boldsymbol{u}$ from the Keplerian shear flow $u_y^{(0)}$, which, in our local coordinate system, is linear with $u_y^{(0)}(x) = -(3/2)\Omega_0 x$ (Wisdom & Tremaine 1988). Here Ω_0 is the background rotation at the

reference radius R. To ensure that the magnetic field $\boldsymbol{B}$ is solenoidal, we solve for the magnetic vector potential $\boldsymbol{A}$, where $\boldsymbol{B} = \nabla \times \boldsymbol{A}$. The complete set of governing equations are the uncurled induction equation for the magnetic vector potential, the momentum equation, the energy equation, and the continuity equation, which we can write in the form

$$\frac{\mathscr{D}\boldsymbol{A}}{\mathscr{D}t} = \boldsymbol{u} \times \boldsymbol{B} + \frac{3}{2}\Omega_0 A_y \hat{\boldsymbol{x}} - \eta\mu_0 \boldsymbol{J}, \qquad (1)$$

$$\frac{\mathscr{D}\boldsymbol{u}}{\mathscr{D}t} = -(\boldsymbol{u}\cdot\nabla)\boldsymbol{u} + \boldsymbol{g} - \frac{1}{\rho}\nabla p + \boldsymbol{f}(\boldsymbol{u}) + \frac{1}{\rho}\boldsymbol{J}\times\boldsymbol{B} + \frac{1}{\rho}\nabla\cdot(2\nu\rho\boldsymbol{S}), \qquad (2)$$

$$\frac{\mathscr{D}e}{\mathscr{D}t} = -(\boldsymbol{u}\cdot\nabla)e - \frac{p}{\rho}\nabla\cdot\boldsymbol{u} + \frac{1}{\rho}\nabla(\chi\rho\nabla e) + 2\nu S^2 + \frac{\eta\mu_0}{\rho}\boldsymbol{J}^2 + Q, \qquad (3)$$

$$\frac{\mathscr{D}\ln\rho}{\mathscr{D}t} = -(\boldsymbol{u}\cdot\nabla)\ln\rho - \nabla\cdot\boldsymbol{u}. \qquad (4)$$

Here, the time derivative $\mathscr{D}/\mathscr{D}t = \partial/\partial t + u_y^{(0)}\partial/\partial y$ includes the transport by the Keplerian shear flow. This is the only place where $u_y^{(0)}(x)$ occurs explicitly. On the right-hand sides of equation (1) and (2) only its gradient $du_y^{(0)}/dx = -(3/2)\Omega_0$ (which is constant) occurs. Originally, there was an explicit $u_y^{(0)}(x)$ dependence in equation (1) because of a term $\boldsymbol{u}^{(0)}\times\boldsymbol{B}$. However, for this term we made use of the identity

$$(\boldsymbol{u}\times\boldsymbol{B})_i = \nabla_i(\boldsymbol{u}\cdot\boldsymbol{A}) - (\boldsymbol{u}\cdot\nabla)A_i - A_j\nabla_i u_j, \qquad (5)$$

and adopted a gauge that removes the gradient term, $\nabla(\boldsymbol{u}\cdot\boldsymbol{A})$, which does not change $\boldsymbol{B}$. The remaining two terms are then an advection term and a term involving only the (constant) gradient of $u_y^{(0)}$. Equation (1) can be verified by taking the curl, which gives the ordinary induction equation.

The term $\boldsymbol{f}(\boldsymbol{u}) = \Omega_0(2u_y, -\frac{1}{2}u_x, 0)$ describes epicyclic deviations from purely circular rotation. This arises from the Coriolis force and part of the inertia force $u_x du_y^{(0)}/dx = -(3/2)\Omega_0 u_x$. In the vertical direction gravity is $\boldsymbol{g} = -\Omega_0^2 z$. These terms arise from locally linearizing about the Keplerian motion. The other remaining quantities have their usual meanings: $\boldsymbol{J} = \nabla\times\boldsymbol{B}/\mu_0$ is the current density, μ_0 the vacuum permeability, η the magnetic diffusivity, χ the thermal diffusivity, and $S_{ij} = \frac{1}{2}(u_{i,j} + u_{j,i} - \frac{2}{3}\delta_{ij}u_{k,k})$. We assume a perfect gas and write the pressure as $p = (\gamma - 1)\rho e$, with $\gamma = 5/3$.

In equation (3) we allow for the possibility of thermal relaxation within the box via the term

$$Q = -\sigma_{\text{cool}}(e - e_0), \qquad (6)$$

where σ_{cool} is a thermal relaxation rate, and e is the internal energy per unit mass. The subscript 0 refers to the initially uniform value (which is determined by the scale height of the disk; see below). In those cases where we include this thermal relaxation effect we assume the cooling rate to be of the order of the rotation rate, $\sigma_{\text{cool}} = \Omega_0$. (A 10 times smaller value of σ_{cool} proved insufficient to prevent secular heating of the disk.)

We also investigate the effect of partial ionization, which is relevant for protostellar disks. Ion pressure and inertia can usually be neglected, and we can therefore account for this effect, known as ambipolar diffusion, by adding in equation (1) the induction $\boldsymbol{u}_D \times \boldsymbol{B}$ due to the ion-neutral drift velocity

u_D, where

$$u_D = (a_{AD}/\rho^{1+n}) J \times B \qquad (7)$$

(e.g., Zweibel 1987). Here, $a_{AD} = (k\gamma_D)^{-1}$, where γ_D is the drag coefficient for ion-neutral collisions, and we have assumed that the ion density can be written as $\rho_i = k\rho^n$, where $n = \frac{1}{2}$ when ionization-electron recombination balances cosmic-ray ionization (e.g., Elmegreen 1979). This leads not only to an increase of the effective magnetic diffusion, but also makes it anisotropic. The effect of ambipolar diffusion on the Balbus-Hawley instability has been investigated analytically by Blaes & Balbus (1994) and numerically by Mac Low et al. (1995).

2.2. *Boundary Conditions*

We apply stress-free, insulating boundary conditions in the z-direction at the top and bottom, i.e., $\partial u_x/\partial z = \partial u_y/\partial z = u_z = \partial e/\partial z = 0$. In terms of A the vertical magnetic field condition is $\partial A_x/\partial z = \partial A_y/\partial z = A_z = 0$. In the toroidal ($y$-) direction we assume periodic boundary conditions. In the radial (x-) direction we adopt for all variables quasi-periodic boundary conditions that account for the effect of the Keplerian shear in the toroidal (y-) direction:

$$F(L_x, y, z) = F(0, y + \tfrac{3}{2}\Omega_0 L_x t, z) \qquad (8)$$

(Wisdom & Tremaine 1988), where F stands for the eight dependent variables and L_x is the radial extent of the box. In other words, the flow is periodic with respect to a position in y that is sliding in time with the local Keplerian shear speed. Such sliding boundary conditions were originally proposed in the context of stellar dynamics, but are now also used in the context of accretion disks (Hawley & Balbus 1992).

For periodic and quasi-periodic boundary conditions in the horizontal directions, the vertical flux vanishes, because

$$\int B_z \, dx \, dy = \int A_y \, dy \Big|_0^{L_x} - \int A_x \, dx \Big|_0^{L_y} = 0 . \qquad (9)$$

For the horizontal fluxes no such restrictions exist, because A_x and A_y in general have different values on the upper and lower boundaries.

2.3. *The Code*

We solve the governing equations using sixth-order compact derivatives (Lele 1992) and a third-order Hyman (1979) scheme for the time stepping. Earlier versions of the code were described by Nordlund & Stein (1990), Brandenburg et al. (1990, 1995), and Nordlund et al. (1992). We adopt artificial viscosities to capture shocks and hyperviscous fluxes to stabilize rapid advection while keeping unphysical distortions to a minimum. The shock capturing viscosity is nonvanishing and proportional to $-\nabla \cdot u$ only in those regions where $-\nabla \cdot u > 0$. The hyperviscosity is proportional to the modulus of the ratio of the third to the first derivative.

It turns out that the flow is much smoother in the toroidal direction than in the vertical and radial directions, and we therefore adopt a nonuniform grid aspect ratio with $\delta x < \delta z < \delta y$. The artificial viscosity, ν_j, depends on the mesh width, and therefore on the direction $j = 1, \ldots, 3$. By symmetrizing the viscous stress tensor, $\nu_j u_{i,j} + \nu_i u_{j,i}$, we make sure that no spurious rotation is introduced in the flow (Batchelor 1967, p. 11).

We validated the code using standard hydrodynamical and MHD shock tube tests, two-dimensional blast waves, advec-

tion tests, and Alfvén pulses. The sliding boundary conditions were tested by advecting temperature and magnetic field perturbations along epicyclic orbits. The ambipolar diffusion part was tested by calculating an oblique C-shock, for which a semi-analytic solution exists (Mac Low et al. 1995). We also reproduced published simulations of the Balbus-Hawley instability (Hawley & Balbus 1991, 1992). Our choice of parameters matches that of Stone & Hawley (1995), and we verify their basic results, although they actually used periodic boundary conditions in the vertical direction.

One time step takes ~ 1.8 s on a Cray-YMP ($\sim 50\%$ is spent on the shock capturing and artificial viscosities). A single run covering 100 orbits requires 5×10^5 time steps, corresponding to 250 cpu hours.

2.4. *Nondimensionalization and Parameters*

We assume an initial isothermal stratification with $e = e_0$, which leads to a Gaussian density profile with

$$\ln \rho = \ln \rho_0 - z^2/H_0^2 . \qquad (10)$$

The value of H_0 determines the isothermal sound speed $c_s = H_0 \Omega_0/2^{1/2} = [(\gamma - 1)e_0]^{1/2}$, where e_0 is the initial uniform value of e. In those cases where $\sigma_{cool} = 0$ the gas in the box will heat, because of Ohmic and viscous dissipation together with insulating boundary conditions. Thus, in those cases H will increase with time.

We measure length in units of the initial vertical scale height of the disk, $[x] = H_0$, time in units of $[t] = (GM/H_0^3)^{-1/2}$, density in units of the initial density at the midplane $[\rho] = \rho_0$, and the magnetic field in units of $[B] = [u](\mu_0 \rho_0)^{1/2}$, where $[u] = [x]/[t]$ is our velocity unit. Here, G is the gravitation constant and M the mass of the central object. Since $GM/R^3 = \Omega_0^2$, we can also write $[t] = (H_0/R)^{3/2}\Omega_0^{-1}$. We thus adopt dimensionless quantities by putting

$$H_0 = GM = \rho_0 = \mu_0 = 1 . \qquad (11)$$

Below we quote times in units of the rotation period $T = T_{rot} = 2\pi/\Omega_0$.

In order to facilitate comparison with Stone & Hawley (1995) and other previous work we adopt the same parameters and initial conditions as they did, unless stated otherwise. The distance from the central object is $R = 100$, corresponding to $\Omega_0 = 10^{-3}$, and the box has an aspect ratio of $L_x:L_y:L_z = 1:2\pi:4$. (This corresponds to an azimuthal wavenumber of $m = 2\pi R/L_y = 100$ which, apart from the average value $m = 0$, is the smallest wavenumber resolved.) For the velocity we take random perturbations such that the initial Mach number is $Ma = u_{rms}/c_s = 0.002$. For the magnetic field we assume $B = \hat{z} B_0 \sin(2\pi x/L_x)$, and determine B_0 such that the plasma beta is $\beta = 2\mu_0 p/B_0^2 = 100$. The numerical resolution is varied between $28 \times 64 \times 65$ and $63 \times 63 \times 127$ mesh points.

Most of the diffusion comes from the artificial viscosities, which are (for the low-resolution case) typically $(0.5-2) \times 10^{-6}$ for the hyperviscosity and $(0-5) \times 10^{-5}$ for the shock viscosity. We still keep the ordinary viscosities, but make them so small that they are practically unimportant ($\nu = \chi = \eta = 10^{-7}$). For orientation, the effective Reynolds number, based on the artificial viscosity and the turbulent root mean square velocity, is ~ 100. The Reynolds number for the Keplerian motion is ~ 700, and the Reynolds number based on the Taylor microscale and the turbulent motions is between 10 and 20.

3. RESULTS

3.1. *Long-Term Evolution*

We first consider the volume averaged kinetic and magnetic energy densities, $\frac{1}{2}\langle \rho u^2 \rangle$ and $\frac{1}{2}\langle B^2 \rangle$, respectively (Fig. 1).

Our longest run covers ~ 120 orbits. No cooling was included, which resulted in a continuous heating of the disk, whose temperature eventually exceeded 10 times its original value. It is plausible that this increase in thermal energy leads to a secular growth of magnetic and kinetic energies (cf. Fig. 1), which then accelerates the rate of heating even more. After $t = 120$ orbits we continued the simulation with cooling turned on.

One hundred twenty orbits appears to be a rather long time span, and yet we continue to find long-term changes in the activity level of the system; see Fig. 1. The evolution of the magnetic energy agrees in several ways with that of Stone & Hawley (1995), even though they used different (i.e., periodic) boundary conditions in the vertical direction. After about one orbit the magnetic energy begins to grow exponentially and reaches a maximum after three orbits. At later times the magnetic energy varies in the range $\frac{1}{2}\langle B^2 \rangle = 10^{-9}–10^{-7}$.

In addition to the curves of $\frac{1}{2}\langle \rho u^2 \rangle$ and $\frac{1}{2}\langle B^2 \rangle$, Figure 1 also shows the contributions from the three directions. The dominant component of the magnetic field is the toroidal, B_y, field. The amplitude of the mean magnetic field is $|\langle B_y \rangle|_{\max} \approx 10^{-4} \approx 0.7 \langle B^2 \rangle^{1/2}$ (cf. Figs. 1 and 2). In the present case the maximum magnetic energy density is comparable to (and frequently greater than) the gas pressure, even though on average $\frac{1}{2}\langle B^2 \rangle \ll \langle \rho e \rangle$.

The ratios between kinetic, magnetic, and thermal energies are $\langle \rho u^2 \rangle / \langle B^2 \rangle \approx 0.15$ and $\frac{1}{2}\langle B^2 \rangle / \langle \rho e \rangle = 0.01–0.1$. Thus, unlike the solar dynamo, our accretion disk dynamo is characterized by superequipartition of magnetic relative to kinetic energy. The ratio of kinetic to magnetic energy changes relatively little while the total activity level changes by more than a factor of 10. This illustrates the close coupling between the turbulence and the magnetic field. There is no close relation between the magnetic and thermal energies, however.

We find that during the evolution the total toroidal flux in the system changes sign in an apparently cyclic manner with a typical half-period of 20–30 orbits. Our simulation is of course too short to be sure that these cycles really persist. Although

we did not expect to find a quasi periodic time dependence, we note that cycles in accretion disk dynamos have previously been found in the framework of mean field theory (e.g., Stepinski & Levy 1988; Torkelsson & Brandenburg 1994). In Figure 2 we plot the three components of the velocity and the magnetic field averaged over the entire domain. Clearly, the y component of the magnetic field shows significant long-term oscillations, while the other components show only smaller variations. During decaying phases (e.g., between $t/T = 65–73$) $\langle B_z^2 \rangle$ shows rapid oscillations with a period of ~ 0.67 orbits. The velocity does not exhibit similarly ordered behavior, although there are occasionally strong acoustic resonance oscillations in the horizontal velocity components with a period $L_z/c = 0.70 T_{\rm rot}$, where $c = H\Omega_0(\gamma/2)^{1/2}$ is the adiabatic speed of sound. These oscillations are distinct from those seen simultaneously in $\langle B_z^2 \rangle$, whose period is $0.67 T_{\rm rot}$; see Figure 1.

In Figure 3 we illustrate the space-time dependence of the horizontally averaged magnetic field. Note again the long-term cyclic behavior and the remarkable coherence above and below the disk plane. The field is of approximately even parity with respect to the midplane. This is also a typical feature of mean field dynamos operating in disk geometry.

From the point of view of dynamo theory, there is an interesting and peculiar property in that the onset of dynamo action is a nonlinear problem, i.e., no kinematic approach is possible, because the velocity in the induction equation is a function of the magnetic field. Furthermore, if the whole process is triggered by the Balbus-Hawley instability a finite amplitude magnetic field is required. Only in the absence of diffusion does the Balbus-Hawley instability operate in the limit of vanishing magnetic field. The weaker the magnetic field, the smaller is the typical wavelength $\lambda_{\rm BH}$ of the Balbus-Hawley instability ($\lambda_{\rm BH} \sim v_A/\Omega_0$, where v_A is the typical Alfvén speed). When the initial magnetic field is reduced, $\lambda_{\rm BH}$ will eventually be smaller than the resistive cutoff scale. In the simulation, this can be a severe restriction, but in reality the resistive cutoff scale is extremely small.

3.2. *Models with Restricted Symmetry*

We used a computational domain restricted to the upper disk plane, to study several variations on our standard model. In most of the cases we used the same boundary conditions at the midplane as we used before at the outer surfaces, the verti-
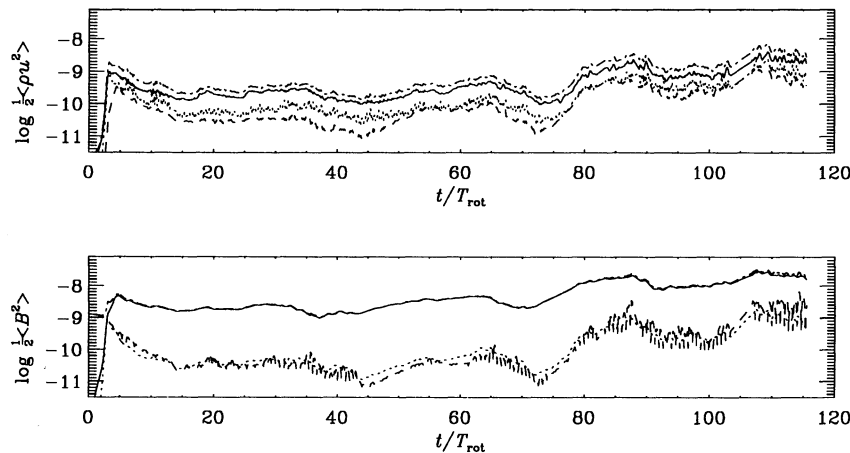

FIG. 1.—Evolution of the logarithm of the averaged kinetic and magnetic energy densities (upper and lower panels, respectively). The energy contained in the x-, y-, and z-components are distinguished by dotted, solid, and dashed lines. The dotted-dashed lines refer to the total energy densities. (Between $t = 103$ and $t = 107$ no data were stored.)
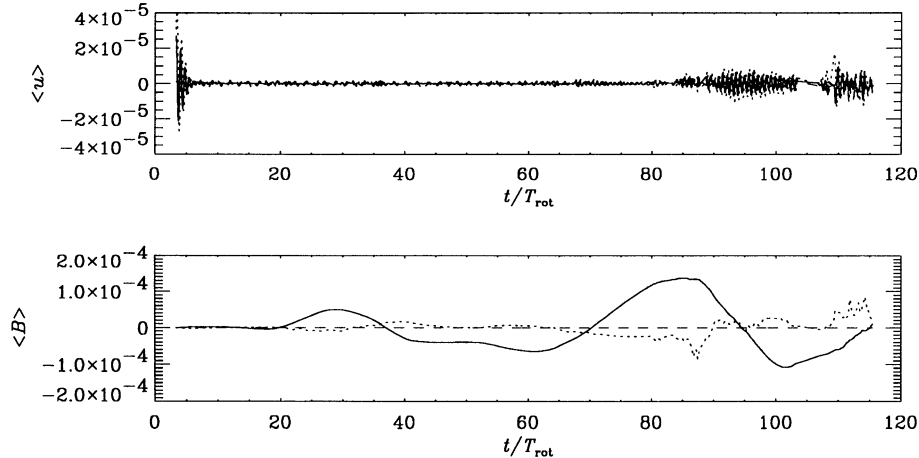
FIG. 2.—The three components of the velocity (*upper panel*) and magnetic field (*lower panel*) averaged over the full box. *Solid line: y, dotted line: x, dashed line: z.* In the lower panel, the $\langle B_x \rangle$ component (*dotted line*) is scaled by a factor of 20, and $\langle B_z \rangle = 0$ exactly.

cal field condition, which imposes a dipolar parity on the magnetic field. We also performed some simulations using a perfect conductor boundary condition at the midplane, i.e., $A_x = A_y = \partial A_z/\partial z = 0$, which corresponds to imposing quadrupolar parity on the magnetic field. Turbulence remains excited for both parities, and the average kinetic and magnetic energy densities are similar; compare the curve labeled "2π" in Figure 4 with Figure 1. The amplitude of the large-scale magnetic field was also similar to the previous case with unconstrained parity, i.e., $\langle B \rangle^2/\langle B^2 \rangle \approx 0.5$ during cycle maximum. It is obviously cheaper to compute models in restricted geometry. Since those runs still reflect the basic properties of the flow, we use them in the following to investigate various effects. We refer to the long run displayed in Figures 1–3 as the reference run, and use the field at $t = 85$ as the new initial condition for the experiments below.

3.2.1. *Omitting the Lorentz Force*

If the Lorentz force is omitted, the Balbus-Hawley instability no longer operates. The turbulence that is present in the initial condition (from the reference run at $t = 85$) decays rapidly with an *e*-folding time of less than 2 orbits, which is roughly the viscous diffusion time based on the correlation length of the flow. At later times the flow becomes axisymmetric (no variation in the streamwise direction) with a smooth pattern of regions of positive and negative u_y across the stream. There remains a weak time dependence with a period of about two orbits, indicating the presence of waves that can be seen by

monitoring the density stratification in time. The flow becomes so smooth that the corresponding turbulence decay rate is drastically reduced.

3.2.2. *Effect of the Geometrical Extent*

We checked how sensitive the model is to changes in the toroidal and radial extent. In our reference model we used $L_y = 2\pi$. We then chopped off the second part of the box and continued the run with $L_y = \pi$; see the curve labeled "π" in Figure 4. After some strong initial readjustments (which occurred because we restarted from a field that was no longer periodic in the y-direction) the kinetic and magnetic energies continued to fluctuate about the same values as in the previous run. However, in this particular run the large-scale magnetic field did not show cycles any more. Thus, at least for $L_y < 2\pi$ finite size effects become important. We also performed a run with $L_x = 2$ and $L_y = 2\pi$ and found qualitatively and quantitatively similar behavior as for $L_x = 1$.

3.2.3. *Effect of Ambipolar Diffusion*

Protostellar disks are only partially ionized, and it is therefore important to include the effects of ambipolar diffusion. We performed two runs for even parity (AD: $a_{AD} = 100$, AD3: $a_{AD} = 500$), and two for odd parity (AD1: $a_{AD} = 10$, AD2: $a_{AD} = 100$). Also, in runs AD and AD3 we used $L_y = 2\pi$, whereas for runs AD1 and AD2 $L_y = \pi$. Only in the small diffusion cases (AD and AD1) does the turbulence remain self-sustained. Stronger ambipolar diffusion (AD2 and AD3) makes the turbulence die out and produces in the end a smooth
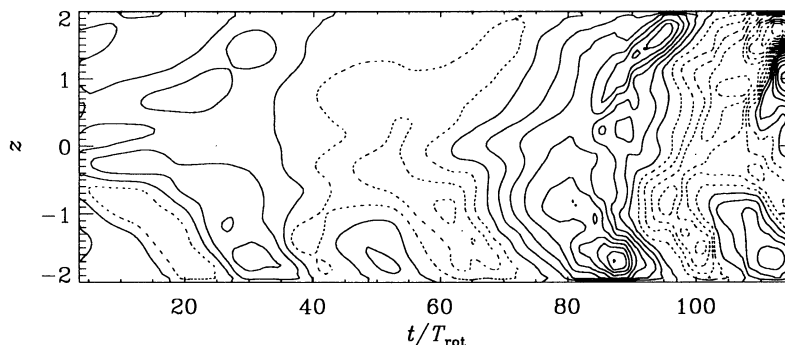

FIG. 3.—Contours of the toroidal magnetic flux vs. time and height. Note the cyclic variation and the even parity of the field.
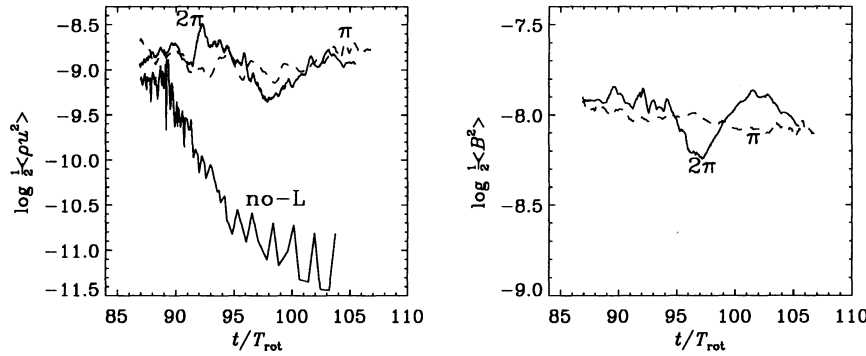
FIG. 4.—The evolution of the kinetic energy in a model covering only the upper disk plane. The symbols 2π and π refer to two different aspect ratios ($1:2\pi:2$ and $1:\pi:2$, respectively). The curve labeled "no-L" gives the evolution for a run with no Lorentz force.

axisymmetric toroidal flow, for which the dissipation rate is minimized (this is why the decay slows down after some time).

The Balbus-Hawley instability operates only if the neutral-ion collision frequency exceeds the angular velocity, i.e., $\nu_{ni} > \Omega_0$ (Blaes & Balbus 1994). In our units, $\nu_{ni} = \rho^{1/2}/a_{AD}$. For $a_{AD} = 500$ we have $\langle\nu_{ni}\rangle \approx \Omega$, and run AD3 shows that this value is too large to sustain the turbulence. On the other hand, for $a_{AD} = 100$ we have $\langle\nu_{ni}\rangle/\Omega \approx 6$, in which case the turbulence remains excited (run AD). Thus, our runs are consistent with the criterion of Blaes & Balbus. For run AD2, where we also used $a_{AD} = 100$, the turbulence decayed. This may be either because the field was forced to be of dipolar parity, or because of the smaller toroidal extent (or both).

Ambipolar diffusion changes the structure of the magnetic field. It acts to minimize the Lorentz force (cf. Brandenburg & Zweibel 1994). Since the dynamo generates magnetic fields only by doing work against the Lorentz force (e.g., Krause & Rädler 1980), this tendency of ambipolar diffusion quenches the source of the dynamo. We find that in run AD ambipolar diffusion leads to a clear increase in the probability that J and B are parallel (Fig. 5), illustrating the tendency of the magnetic field to be close to a force-free configuration in the presence of ambipolar diffusion.

Our simulations do not show evidence for ambipolar diffusion sharpening magnetic structures, which has been found for one and two-dimensional flows (e.g., Brandenburg & Zweibel 1994; Mac Low et al. 1995). This may be due to the fact that the effective magnetic diffusion in the code is comparable to the ambipolar diffusion, $\lambda_{AD} = v_A^2/\nu_{ni}$, or because the ambipolar diffusion time, $\tau_{AD} = H^2/\lambda_{AD}$ is long compared with the lifetime of turbulent structures or the rotation time. (For run AD, $\Omega\tau_{AD} \approx (c_s/v_A)^2(\nu_{ni}/\Omega) \approx 30 \gg 1$.) Nevertheless, the peculiar depencence of ambipolar diffusion on the Lorentz force makes its effect visible even on the background of a comparable effective numerical diffusion.
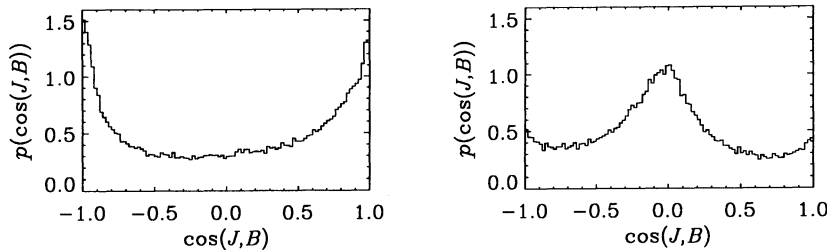
3.2.4. Radius Dependence

All the simulations presented above have been obtained for one particular radius ($R = 100$ in our units). It is clear, however, that the disk parameters change with radius. In order to check whether the properties of our model are sensitive to the radial position, we apply our model at a radius 5 times smaller. We choose $\Omega_0 = 10^{-2}$, corresponding to $R = 21$, and we scale the density and scale height according to the Shakura-Sunyaev model (e.g., Frank, King, & Raine 1992), i.e., $\rho_0 \propto R^{15/8}$ and $H_0 \propto R^{9/8}$, so $\rho_0 = 0.056$ and $H_0 = 0.18$. (We thus keep the nondimensionalization [11] of the old reference radius $R = 100$.)

We rescaled a snapshot from a run obtained for $R = 100$ and ran it for several orbits. The maximum kinetic and magnetic energy densities are again close to equipartition (even though the averages are not). The maximum Mach number is generally above unity. In Table 1 we compare further details of models with different radii. Unlike the short model in § 3.2.2, the toroidal magnetic field did show cyclic behavior, even though we used $L_y/L_x = \pi$ for these models.

3.3. Energetics

In order to investigate the process of dynamo-generated turbulence in more detail, consider the magnetic, kinetic, and thermal energy equations,

$$\frac{d}{dt}\left\langle\frac{1}{2\mu_0}B^2\right\rangle = -\frac{3}{2}\Omega_0\frac{1}{\mu_0}\langle B_x B_y\rangle$$
$$- \langle u\cdot(J\times B)\rangle - \langle\eta\mu_0 J^2\rangle, \quad (12)$$

$$\frac{d}{dt}\left\langle\frac{1}{2}\rho u^2\right\rangle = \frac{3}{2}\Omega_0\langle\rho u_x u_y\rangle + \langle\rho u\cdot g\rangle$$
$$- \langle u\cdot\nabla p\rangle + \langle u\cdot(J\times B)\rangle - \langle 2\nu\rho S^2\rangle, \quad (13)$$

FIG. 5.—Probability density functions of the cosines of the correlation angles between J and B with (left) and without (right) ambipolar diffusion (runs AD and C, even parity, $L_y = 2\pi$). With diffusion J and B are more likely to be parallel, corresponding to force-free regions.

TABLE 1

COMPARISON OF VARIOUS MODELS WITH/WITHOUT COOLING AND CONSTRAINED/FREE PARITIES

	RUN						
PARAMETER	A	B	C	D	E1	E2	AD
Cooling....................	Yes	Yes	Yes	No	No	No	Yes
Parity........................	Odd	Odd	Even	Odd	Free	Free	Even
H_0	0.18	1.00	1.00	1.00	1.00	1.00	1.00
Ω_0..........................	10^{-2}	10^{-3}	10^{-3}	10^{-3}	10^{-3}	10^{-3}	10^{-3}
$\langle\rho\rangle$	0.022	0.48	0.48	0.48	0.48	0.48	0.48
α_{SS}^{mag}	0.0015	0.0007	0.0041	0.0014	0.0035	0.0023	0.0031
α_{SS}^{kin}	0.0005	0.0002	0.0010	0.0003	0.0005	0.0003	0.0007
E_{mag}/E_0	0.013	0.014	0.05	0.014	0.023	0.017	0.05
E_{kin}/E_{mag}	0.23	0.11	0.13	0.20	0.15	0.14	0.09
$\frac{3}{2}\langle B_x B_y\rangle/\langle\frac{1}{2}B^2\rangle$	0.25	0.11	0.21	0.22	0.32	0.28	0.14
$\frac{3}{2}\langle\rho u_x u_y\rangle/\langle\frac{1}{2}B^2\rangle$	0.07	0.03	0.05	0.06	0.05	0.04	0.03
$\langle u\cdot(J\times B)\rangle/\langle\frac{1}{2}B^2\Omega\rangle$	0.14	0.06	0.05	0.13	0.15	0.19	-0.02
λ_{BH}/H	0.94	0.21	0.37	0.27	0.40	0.25	0.38
λ_K/H	0.13	0.12	0.17	0.13	0.13	0.13	0.20
λ_M/H	0.17	0.26	0.18	0.19	0.17	0.18	0.27
$2\Omega H/\langle u^2\rangle^{1/2}$	16	20	9	16	13	25	22
$\langle\omega_x^2\rangle/\langle\omega^2\rangle$	0.19	0.20	0.25	0.22	0.23	0.20	0.12
$\langle\omega_y^2\rangle/\langle\omega^2\rangle$	0.24	0.26	0.26	0.27	0.23	0.22	0.37
$\langle\omega_z^2\rangle/\langle\omega^2\rangle$	0.57	0.54	0.49	0.51	0.54	0.58	0.51

NOTES.—Run A applies to a 5 times smaller radius from the central object compared to the other runs. For run E we have given averages taken separately over the last $\frac{3}{4}$ of the run (E1) and over the full run (E2). $E_0 = \frac{3}{4}\Omega_0^2 H^2\langle\rho\rangle$ is the thermal energy of the initial state. The three length scales, λ_{BH}/H, λ_K/H, and λ_M/H are explained and discussed in § 3.6.

$$\frac{d}{dt}\langle\rho e\rangle = -\langle p\nabla\cdot u\rangle + \langle\eta\mu_0 J^2\rangle + \langle 2\nu\rho S^2\rangle + \langle\rho Q\rangle . \quad (14)$$

Here we have made use of the fact that neither the vertical field condition nor the perfect conductor condition permit a Poynting flux through the surface. The artificial viscosities have not been explicitly included in equations (12)–(14), but these terms are roughly similar to those involving ordinary viscosities. The work done against and by the gravity, $\langle\rho u\cdot g\rangle$, leads to an exchange between potential energy, $\langle\rho z\cdot g\rangle$, and kinetic energy.

The equation for the total energy (the sum of kinetic, magnetic, thermal, and potential energies) is

$$\frac{d}{dt}E_{tot} = \frac{3}{2}\Omega_0\left(\langle\rho u_x u_y\rangle - \frac{1}{\mu_0}\langle B_x B_y\rangle\right) + \langle\rho Q\rangle . \quad (15)$$

The first two terms arise from the work done against the advection and Lorentz forces. These terms are balanced by the cooling term or, if $Q = 0$, lead to continuous heating of the box. In most of our runs we have $Q = 0$, and consequently we find a significant increase of temperature during the run.

Energy flows from the Keplerian motion into both magnetic and kinetic energies (Fig. 6), but ~6 times more energy goes into the magnetic energy as into the kinetic energy. However, since the kinetic energy is much smaller than the magnetic energy, the energy transfer rates (the energy flux divided by the corresponding energy content) into the two energy reservoirs are approximately equal (i.e., $\approx 0.3\Omega$). Moreover, the Lorentz force pumps half of this magnetic energy into kinetic energy, in contrast to convectively driven dynamos where work is done against the Lorentz force. As a result, $\frac{3}{4}$ of the energy going from the Keplerian motion into the turbulence first passes through a phase of magnetic energy and then goes into the kinetic energy of the turbulence. Most of the heating of the disk comes from viscous rather than Ohmic heating, even though most of the rotational energy is converted first into magnetic energy, because the turbulence is driven by the Lorentz force. On a global picture, the role of the kinetic and magnetic energy reservoirs is that of a catalyst that allows us to tap the energy in the Keplerian flow. However, neither the turbulence nor the dynamo alone are able to do this conversion. The two have to work together.

It is clear that the dynamo cannot work with Keplerian shear alone—a weak radial magnetic field is needed for the Keplerian shear to act. However, since the poloidal magnetic energy is small compared to the toroidal magnetic field, only a small amount of kinetic energy is required for the turbulence to replenish the subreservoirs $\langle B_x^2\rangle$ and $\langle B_z^2\rangle$. We find that this happens at a rate comparable to the growth rate of the Balbus-Hawley instability or, more specifically,

$$\left.\frac{d\ln\langle B_x^2\rangle}{dt}\right|_{str} \approx \left.\frac{d\ln\langle B_z^2\rangle}{dt}\right|_{str} \approx 0.6\Omega_0 , \quad (16)$$
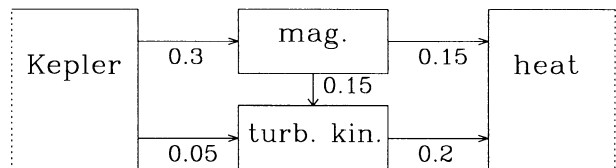

FIG. 6.—Sketch of the energy budget. Energy is tapped from the Keplerian motion and goes into magnetic and kinetic energy, and is finally converted into heat. The numbers give the approximate energy fluxes in units of $\langle\frac{1}{2}B^2\Omega\rangle$.

where the subscript "str" refers to the gain (or loss) from the stretching term $(\boldsymbol{B} \cdot \nabla) u_i$ in the directions $i = x, z$. Although these terms are crucial for the operation of the dynamo, they are relatively unimportant for the energy budget. Indeed, once the magnetic field is stretched into toroidal flux tubes, magnetic energy goes back into kinetic energy (especially the z-component) via work done by the vertical magnetic pressure gradient, $\langle u_z \nabla_z(\frac{1}{2}\boldsymbol{B}^2)\rangle$. It is the resulting vertical motions that feed back into driving vertical magnetic field fluctuations by deforming the toroidal magnetic field. Most of the $\langle B_x^2 \rangle$ field is regenerated via $\langle u_x^2 \rangle$, which is driven mostly by work done by the restoring force in the radial direction (the epicyclic term). It is suggestive to ascribe this effect to the Balbus-Hawley instability, although other mechanisms may also operate. For example, the generation of vertical fields is reminiscent of the Parker instability, although this description may be too simplistic, especially because rotation can significantly reduce the growth rate of the Parker instability (Zweibel & Kulsrud 1975; Parker 1975; Cattaneo & Hughes 1988; Foglizzo & Tagger 1994).

3.4. Turbulent Transport

Our local model does not allow any actual transport through the disk, because $\langle \rho u_x \rangle$ vanishes on the average. This is a consequence of neglecting curvature effects, which makes the inward and outward directions indistinguishable. In a real accretion disk angular momentum is transported by the Reynolds and Maxwell stresses, which are commonly parameterized in terms of turbulent viscosities, v_t^{kin} and v_t^{mag}, via

$$\langle \rho u_x u_y \rangle = \tfrac{3}{2}\Omega_0 \, v_t^{\text{kin}}\langle \rho \rangle \,, \tag{17}$$

$$-\frac{1}{\mu_0}\langle B_x B_y \rangle = \frac{3}{2}\,\Omega_0 \, v_t^{\text{mag}}\langle \rho \rangle \,. \tag{18}$$

Here we made use of the fact that, in cylindrical polar coordinates, $r\,\partial\Omega/\partial r = -(3/2)\Omega$, and the turbulent viscosity parameters, v_t^{kin} and v_t^{mag}, can be nondimensionalized by

$$v_t^{\text{kin}} = \alpha_{\text{SS}}^{\text{kin}} c_s H \,, \quad v_t^{\text{mag}} = \alpha_{\text{SS}}^{\text{mag}} c_s H \,, \tag{19}$$

where the subscript SS refers to Shakura & Sunyaev (1973), who used this prescription the first time to compute models of accretion disks. Even in our local model, although there is no net transport possible, the stress terms are nonvanishing and have the expected sign. This is because the turbulent viscosity also leads to turbulent heating, which is governed by the same turbulent viscosity coefficient. Combining equations (15), (17), and (18), we find

$$\left(\frac{de}{dt}\right)_{\text{diss}} = v_t\left(\frac{3}{2}\,\Omega_0\right)^2 \,, \tag{20}$$

where $v_t = v_t^{\text{kin}} + v_t^{\text{mag}}$. By measuring the temperature increase in our box we have an independent check on the sum of the two turbulent viscosities. We find roughly similar values using the two different methods, i.e., via equations (19) and (20). In Table 1 we summarize the results for different models with and without cooling included.

The total effective Shakura-Sunyaev viscosity parameter, $\alpha_{\text{SS}} = \alpha_{\text{SS}}^{\text{mag}} + \alpha_{\text{SS}}^{\text{kin}}$, varies between 0.001 and 0.005; see Table 1. A similar range of values has also been found by Różyczka & Spruit (1993) using a global two-dimensional simulation of shock driven accretion. Although these are two completely different cases, it is interesting to note that simulations, such as these two, tend to give values of α_{SS} that are significantly below

unity. In our case, such small values result from a number of factors that are all below unity, especially the ratio of magnetic to thermal energy and the normalized correlation $\langle B_x B_y \rangle / \langle \boldsymbol{B}^2 \rangle$.

In Table 1 we also give energy transfer rates (normalized to $\langle \frac{1}{2}\boldsymbol{B}^2 \Omega \rangle$), which are to be compared with the values given in Figure 6. The remaining entries are discussed in § 3.5.

It is difficult to give reasonable error bars for the quantities given in Table 1. The results are obtained by averaging data whose fluctuations are at least comparable to their averages. We expect that, for example, the values of α_{SS} given in Table 1 are uncertain by a factor of ~ 2. In addition, the results may depend on the resolution and this could introduce uncertainty by another factor of 2. The values of α_{SS} obtained in the present work are comparable with the range of values used to construct disk models for active galactic nuclei. However, the values adopted in models for dwarf novae outbursts are typically ~ 0.1 (e.g., Cannizzo, Shafter, & Wheeler 1988), which is at least 20 times the value obtained in our simulations. This discrepancy seems to be too large to be explainable in terms of error bars or numerical effects (resolution, artificial viscosities, or boundary conditions).

3.5. Large-Scale Magnetic Field

A large-scale toroidal, $\langle B_y \rangle$, magnetic field is generated in our simulations (Fig. 7). Note the toroidal flux structures (tubes) with a length comparable to L_y, but relatively small cross section. Most of the magnetic field vectors point to the right (negative B_y), but some vectors (especially below the midplane) point in the opposite direction. On the upper and lower surfaces one sees many flux bundles that are weakly inclined against the torodial direction. The energies of both large- and small-scale magnetic fields exceed the kinetic energy. Thus, the flow is strongly governed by the magnetic field. A strong toroidal field can easily be produced by shearing out a weak radial field. A radial mean magnetic field, $\langle B_x \rangle$, is indeed present in the simulation (see Fig. 2), and its typical value is ~ 100 times smaller than the mean toroidal field, $\langle B_y \rangle$. (The two are roughly in antiphase, as expected for negative shear.) Because of the periodic boundary conditions in x and y, the $\langle B_z \rangle = 0$ field is conserved, and for our initial conditions it vanishes and can therefore not explicitly be involved in the large-scale field regeneration. In order to regenerate $\langle B_x \rangle$ from $\langle B_y \rangle$ we need to have a z-dependent electromotive force in the y-direction, $\langle \mathscr{E}_y \rangle = \langle \boldsymbol{u} \times \boldsymbol{B} \rangle_y$. We are therefore interested in the magnitude of $\langle \mathscr{E}_y \rangle$ and whether there is a correlation between $\langle \mathscr{E}_y \rangle$ and $\langle B_y \rangle$.

For an alpha-omega dynamo, $\langle \mathscr{E}_y \rangle = \alpha_{\text{dyn}}\langle B_y \rangle$. In the usual alpha-effect dynamo (e.g., Krause & Rädler 1980), the field is governed by the fluid motions. We therefore cannot expect that the traditional alpha-omega formalism is valid in the present case, even though the mean magnetic field generated in the simulation shows cyclic migration reminiscent of the dynamo waves typical of many alpha-omega dynamo models (Parker 1979).

There appears to be a correlation between $\langle \mathscr{E}_y \rangle$ and $\langle B_y \rangle$ in Figure 8, with

$$\langle \mathscr{E}_y \rangle = (-2, +4) \times 10^{-3}\langle B_y \rangle\langle \boldsymbol{u}^2 \rangle^{1/2} \,, \tag{21}$$

where the two values in parenthesis are the average values above and below the midplane, respectively. In the upper disk plane the correlation is worse than in the lower disk plane (the
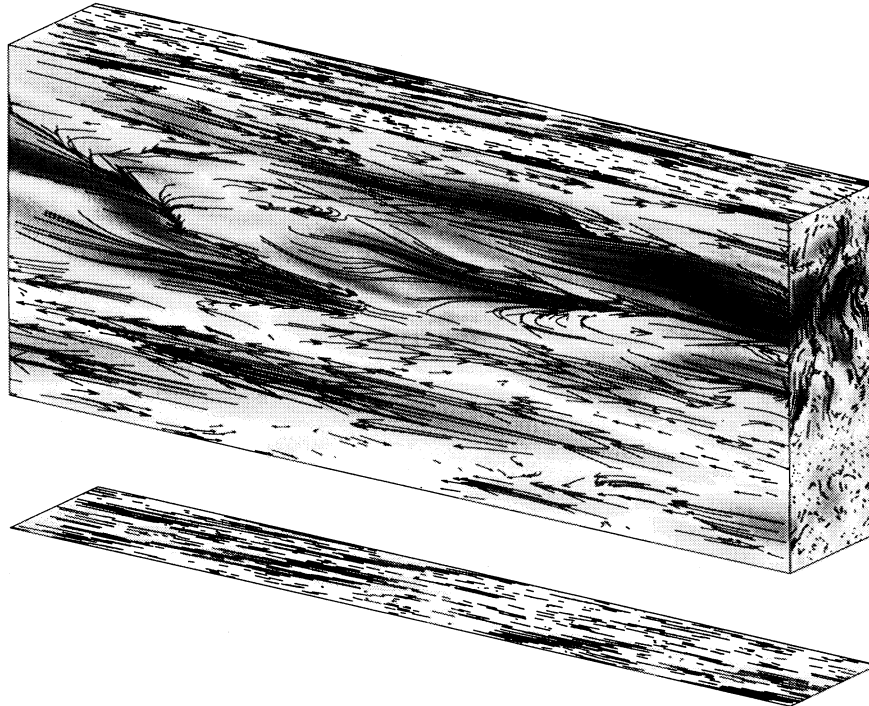
Fig. 7.—Magnetic field lines and a gray-scale representation of the magnetic energy density at the surface of the computational box. Strong magnetic fields are dark. The toroidal direction is to the left. $t/T = 107$.

correlation coefficients for the linear fits shown in Figure 8 are, respectively, -0.19 and 0.76.)

There also appears to be a weak correlation between $\langle \mathscr{E}_x \rangle$ and $\langle B_y \rangle$ with

$$\langle \mathscr{E}_x \rangle = (-4, +4) \times 10^{-2} \langle B_y \rangle \langle u^2 \rangle^{1/2} \qquad (22)$$

above and below the midplane. This term can be interpreted as a vertical transport of the average $\langle B_y \rangle$ field, because we can write equation (22) as $\langle \mathscr{E}_x \rangle = u_B \hat{z} \times \langle B_y \rangle$, where $u_B = (+4, -4) \times 10^{-2} \langle u^2 \rangle^{1/2}$. The sign of u_B corresponds to a transport

of magnetic field away from the midplane. This might be an indication of the effect of magnetic buoyancy.

The ratio of the typical values of $\langle \mathscr{E}_y \rangle$ and $\langle B_y \rangle \langle u^2 \rangle^{1/2}$ in our model is $\sim 4 \times 10^{-3}$. This relatively small value can partly be explained by the tendency of u and B to avoid each other and to be aligned (see the next section). Another important aspect may be that the flow is not fully three-dimensional, a significant amount of energy may be in the form of two-dimensional eddies. In that case only the smaller three-dimensional component of the flow would act as a dynamo.
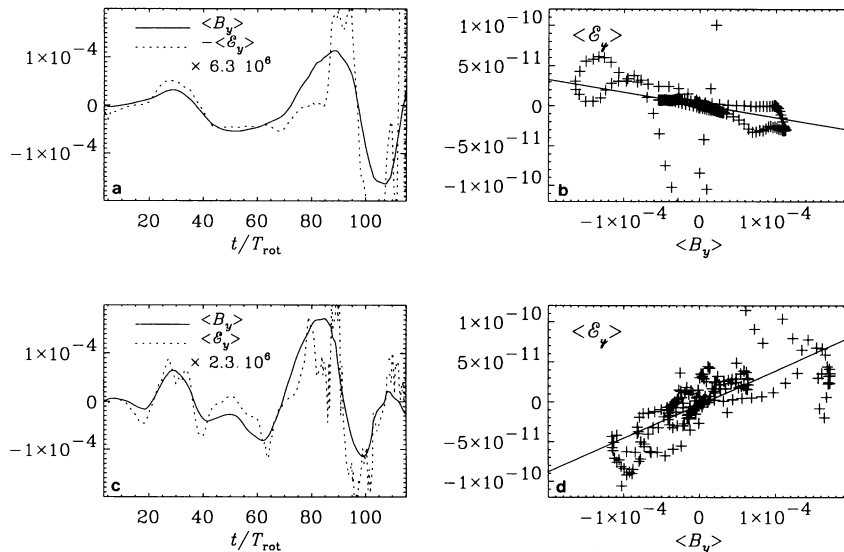

Fig. 8.—Comparison of the evolution of $\langle B_y \rangle$ with $\langle \mathscr{E}_y \rangle$ (a: upper disk plane, c: lower disk plane) and their correlation (b: upper disk plane, d: lower disk plane). Averages are over space (separately above and below the midplane) and over a short time interval of five orbits.

This can be quantified by the magnitude of the enstrophy in the vertical direction relative to the total enstrophy, $\langle \omega_z^2 \rangle / \langle \omega^2 \rangle$. This ratio is unity if the flow is purely two-dimensional and in horizontal planes, and it is $\frac{1}{3}$ under fully isotropic conditions. Table 1 shows that the enstrophy in the vertical direction is more than twice as big as in the two horizontal directions. Further evidence for enhanced two-dimensionality of the flow comes from the fact that the helicity, $\langle \omega \cdot u \rangle$, is weak. (The helicity vanishes for planar two-dimensional motions.) We find that the relative helicity is

$$\frac{\langle \omega \cdot u \rangle}{(\langle \omega^2 \rangle \langle u^2 \rangle)^{1/2}} = \begin{pmatrix} -0.02 \\ +0.05 \end{pmatrix} \qquad (23)$$

above and below the disk plane. (The relative magnetic helicity and the current helicity are less than 20% of the ordinary helicity, and the current helicity has the opposite sign.) The sign of the helicity in equation (23) is consistent with the Coriolis force twisting rising eddies against the overall rotation as they expand into a lower density environment, and descending eddies in the opposite sense as they get compressed in a higher density environment.

There is at present no theory for the large-scale field that is applicable to magnetically dominated turbulence. It is nevertheless instructive to contrast our simulations with conventional alpha-effect dynamo theory (where the turbulence is not dominated by the magnetic field). According to Yoshimura (1975), a migration pattern similar to the one observed here (away from the midplane) is expected when $\alpha_{\mathrm{dyn}} du_y^{(0)}/dx > 0$. Since $du_y^{(0)}/dx < 0$, this would suggest a negative α_{dyn} above the disk plane and a positive sign below, as is indeed the case here (cf. eq. [21]). The effective dynamo number $D = \alpha_{\mathrm{dyn}} \Omega H^3 / \eta_t^2$ (e.g., Parker 1979) is ~ 30, where we estimated the effective

turbulent magnetic diffusivity, η_t, using the Shakura-Sunyaev prescription with $\alpha_{\mathrm{SS}} \sim 0.004$. However, in an ordinary alpha-omega dynamo α_{dyn} and $\langle \omega \cdot u \rangle$ should have opposite signs (e.g., Moffatt 1978). Comparing equations (21) and (23), we see that this is not the case in our simulations. In the theory of Steenbeck, Krause, & Rädler (1966; see also Roberts & Stix 1971), α_{dyn} arises from a vertical gradient in density and turbulent intensity. The two gradients usually have opposite sign, but in our case the density stratification is dominant and their theory is therefore also unable to explain the anomalous sign of α_{dyn}.

We conclude that the mean longitudinal electric field $\langle \mathscr{E}_y \rangle$ (and hence $\langle B_x \rangle$) is not the result of a conventional alpha-effect acting on $\langle B_y \rangle$. Even the causality assumed in the conventional alpha-effect need not be applicable here; the observed correlation between $\langle \mathscr{E}_y \rangle$ and $\langle B_y \rangle$ does not imply that one is the cause of the other. Instead, both could be merely diagnostics of an underlying dynamo mechanism.

It is also possible that the cyclic behavior is facilitated by the finite box size and might be absent in a global model. At least, some of the properties of the mean magnetic field might change drastically if we relaxed the restriction to a local model.

3.6. Flow Structure and Statistics

Abramowicz et al. (1992) proposed that accretion disks could be covered by numerous vortices that would locally increase the emissivity and thus could explain observed brightness variations in active galactic nuclei. It is interesting to look for such vortices in our simulations. In Figure 9 we plot the vertical vorticity and streamlines in a cross section through $z = 1$. The vertical vorticity shows long bands where the sign is the same, while the velocity indicates the formation of vortex-like structures with nearly closed streamlines in places. Magnetic
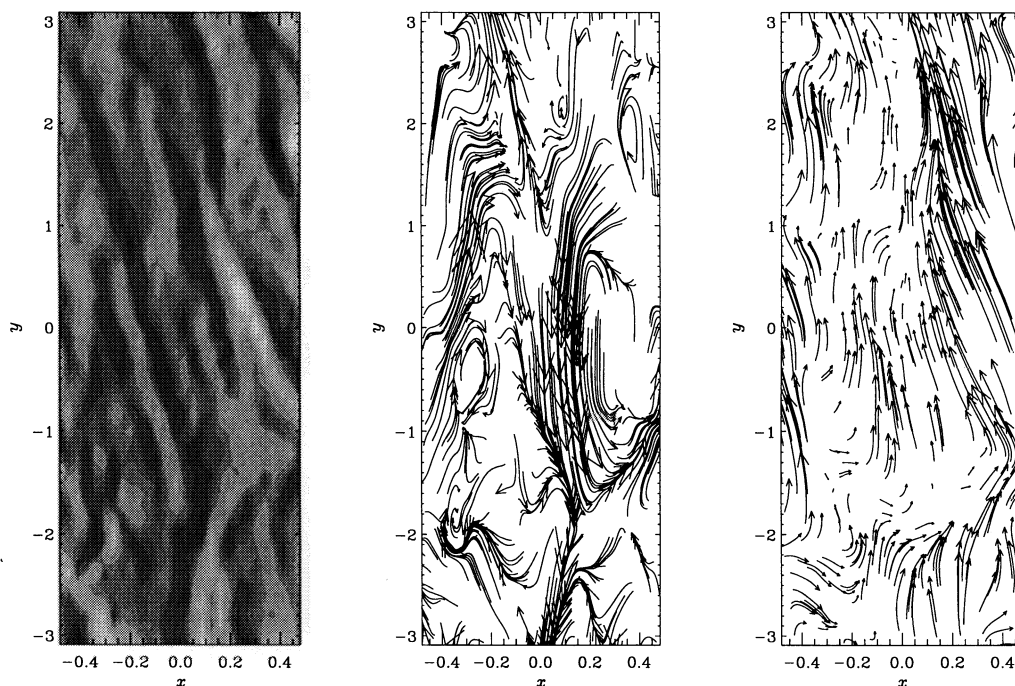

Fig. 9.—Vorticity (left), stream lines (middle), and magnetic field lines (right) in the midplane. Dark means negative vorticity, and light positive vorticity. Stream lines and magnetic field lines are placed randomly, and their length is proportional to the velocity and field strength, respectively. In order to emphasize the deviations from the mostly toroidal orientation of the magnetic field we have divided the B_y by a factor of 5. $t/T = 81.9$.

fieldlines are also plotted, showing that the y component is mostly positive. The B_x field arises mostly near vortex-like structures. By comparing flow pictures at different times, we find that such structures develop rapidly during a single orbit. Thus, in our present model there is no evidence for long-lived vortices, as proposed by Abramowicz et al. (1992). However, the magnetic flux tube structures in our simulation are more long-lived, and it would be natural to invoke them in order to explain the observed brightness variations. Also, we cannot exclude the possibility that long-lived vortices can exist in a modified disk model.

The typical scale of turbulent structures is between the typical scale of the Balbus-Hawley instability, $\lambda_{BH} = \langle v_A \rangle / \Omega$, and the kinematic and magnetic Taylor microscales, $\lambda_K = (5\langle u^2 \rangle / \langle \omega^2 \rangle)^{1/2}$, $\lambda_M = (5\langle B^2 \rangle / \langle J \rangle)^{1/2}$, respectively. The three scales are typically between 0.1 and 0.4; see Table 1. It is interesting to note that in the present case of dynamo-generated turbulence the kinematic and magnetic Taylor microscales are very similar, whereas in convective dynamos the magnetic Taylor microscale is typically smaller than the kinematic one, even when the magnetic and kinematic diffusivities are similar (Brandenburg et al. 1995). The inverse Rossby number, $2\Omega H / \langle u^2 \rangle^{1/2}$, which measure the rotational influence on the turbulence, is always above 10. This indicates that the turbulence is strongly affected by rotation and shear, which leads not only to a strong two-dimensional component of the motions, but also to the helical character of the remaining three-dimensional component; see § 3.5.

The anisotropy of the flow can be quantified by computing one-dimensional power spectra of the velocity and the magnetic field separately for the three directions (Fig. 10). (As for usual power spectra, we sum over all three components of velocity and magnetic field, respectively, but separately for the three directions.) Since the flow is highly anisotropic, we expect the spectra in the three directions to be different. The one-dimensional power spectra of the velocity and the magnetic field (Fig. 10) show that at large scales most of the energy is in structures in the y-direction, and at small scales, the structures are smoother along the y-direction. At small scales, the energy is approximately equally distributed in structures in the x- and z-directions. The fact that the three spectra are continuous indicates that there is no simple (e.g., periodic) flow and magnetic field pattern. From the power spectra in the three directions we have obtained autocorrelation functions via inverse Fourier transformation. For the correlation lengths (halfwidth of the autocorrelation function) we obtained 0.08, 0.5, and 0.16 in the x, y, and z-directions, respectively. These rather dispa-

rate length scales justify the use of different mesh resolution in the three directions.

There are many similarities with other forms of turbulence (e.g., homogeneous and convective), but there are also significant dissimilarities. To quantify this, we now supplement our investigations by a study of various statistical properties.

Probability density functions (PDFs) of u, B, ω, and J are shown in Figure 11. The PDFs are normalized such that their integral is unity. Note that the PDFs of the y components of u and B are much broader than any of the other two components. This reflects again the anisotropy of the turbulence and especially the magnetic field in the streamwise direction. The distribution of u_y is broader than those of u_x and u_z, which is due to that fact that the turbulent eddies are elongated in the y-direction; cf. Figure 9. The ω and J fields show exponential tails (except for J_y), and the distributions of ω_z and J_z are broader than the other distributions. This reflects again the tendency of the flow to be two-dimensional; cf. § 3.5.

The kurtosis of the magnetic field is around 8 in the x-direction and around 4 in the y-direction. Since the kurtosis is a measure of intermittency, this indicates that the B_x field is more intermittent than the B_y field. The skewness of the y-component of the magnetic field changes sharply between -2 and $+2$ during reversals of $\langle B_y \rangle$; see Figure 12. The skewness of the x-component changes roughly between -1 and $+1$ (in antiphase with the skewness of B_y).

In Figure 13 we display PDFs of the cosines of the correlation angles between various vector fields. There is a weak alignment between u and B which is also seen in MHD convection (e.g., Brandenburg et al. 1995). Weak evidence also exists for antialignment of ω and B. For (ω, u) the distribution is rather flat, which is not seen in homogeneous and convective turbulence. However, there is a systematic difference between the upper and lower disk plane, where the net helicities are negative and positive, respectively. The distribution of $\cos (J, B)$ has a peak near zero, which comes from those regions in space where the Lorentz force is acting.

Finally, we investigate the alignment of velocity and magnetic fields with the three eigenvectors (e_1, e_2, e_3) of the rate of strain matrix, $\frac{1}{2}(u_{i,j} + u_{j,i})$; see Figure 14. (Note that u is only the deviation from the Keplerian flow.) The corresponding eigenvalues are ordered such that $\lambda_1 < \lambda_2 < \lambda_3$. The eigenvectors e_1 and e_3 give the directions of compression and stretching, respectively. In ordinary turbulence the vorticity is aligned with the intermediate eigenvector e_2 (Kerr 1987; Ashurst et al. 1987). Our present results also show this alignment. However, the degree of alignment is much more pro-
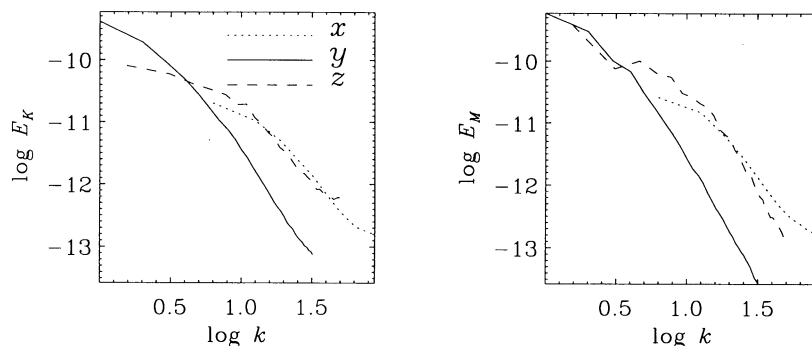

Fig. 10.—Power spectra of the velocity and the magnetic energy in the three directions. $t/T = 107$
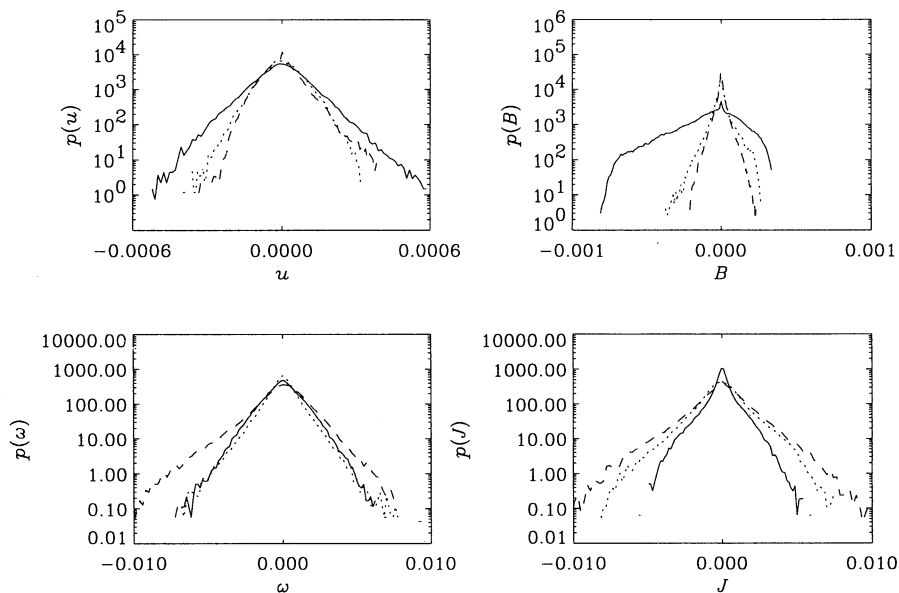
Fig. 11.—PDFs of u, ω, B, and J. The solid lines refer to the y-components, whereas dotted and dashed lines refer to the x- and z-components. $t/T = 107$.
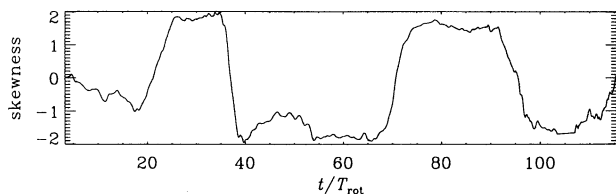

Fig. 12.—Skewness of B_y. Note the sharp changes during field reversals.

nounced here than in ordinary turbulence. These alignment properties do not apply to the magnetic field. Instead, there is an intermediate angle of $\sim 45°$ between B and the directions of compression (e_1) and stretching (e_3).

The fact that there is a 45° angle between the magnetic field

and the directions of stretching and compression is not a peculiarity of the magnetic field, but rather a natural property of any shear flow. A shear flow can be divided into straining and rotational motions. (Fig. 9 shows that even the deviations from the Keplerian motion still show local shear aligned with the toroidal direction.) Since the eigenvectors are orthogonal, e_1 and e_3 must form an angle of 45° with the x- and z-directions. (We confirmed that e_1 and e_3 have indeed high probabilities to be at an angle of 45° with the x- and y-directions.) Furthermore, there is almost perfect alignment of the magnetic field with the toroidal direction (the probability density reached values ~ 40). Consequently, the B-field is a proxy for the y-direction and therefore at an angle of 45° with e_1 and e_3.
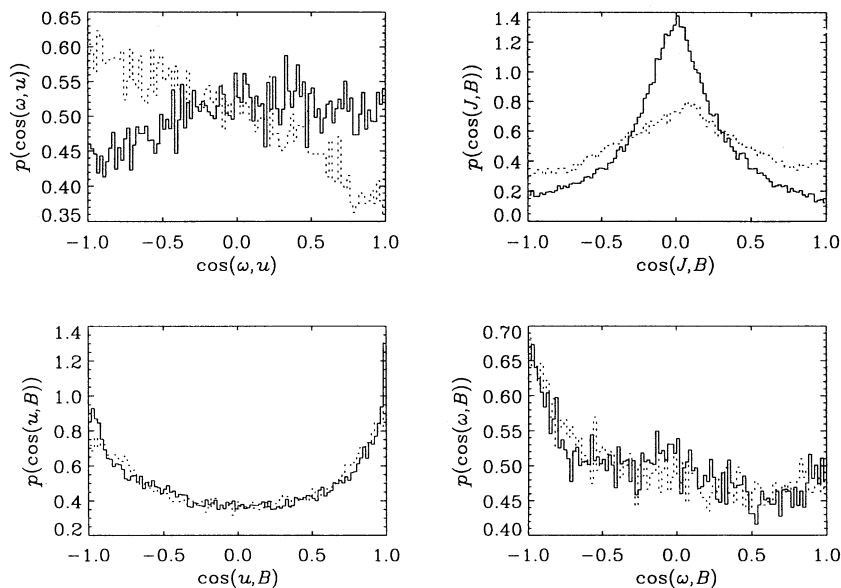

Fig. 13.—PDFs of the cosines of the correlation angles between various vector fields. Solid and dotted lines refer to PDFs taken separately from data points above and below the disk plane. (Note that the scale of the ordinate varies.) $t/T = 107$.
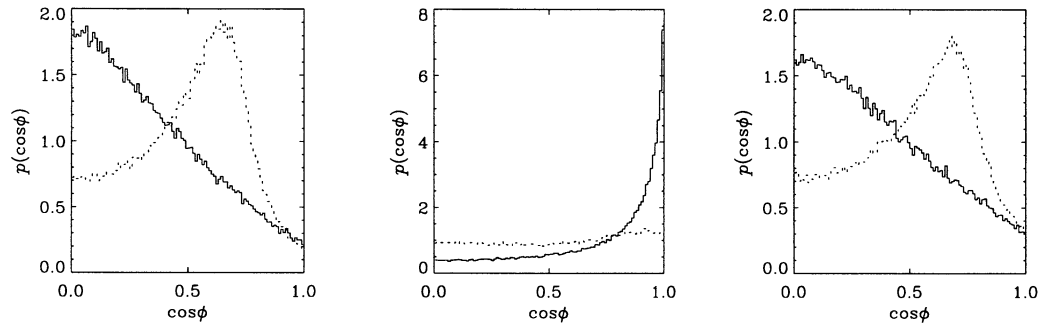
Fig. 14.—PDFs of the cosines of the correlation angles between velocity (*solid lines*) and magnetic fields (*dotted lines*) with the three eigenvectors of the rate of strain matrix (*left*: e_1; *middle*: e_2; *right*: e_3). (Note that the scale of the ordinate varies.) $t/T = 107$.

The intermediate eigenvector is perpendicular to both e_1 and e_3, and in this shear flow it is therefore more nearly aligned with the z-direction which, in turn, is correlated with the vorticity. Thus, the observed alignment properties of vorticity and magnetic field appear naturally in shear flows.

3.7. *Correlation Tensors*

In §§ 3.3 and 3.4 we discussed the significance of the horizontal (x, y) component of the Reynolds and Maxwell stress tensors for the angular momentum transport. Because of the possible observational implications, which were first pointed out by Balbus, Gammie, & Hawley (1994), we now discuss all the tensor components. In our model, where the parity is unrestricted, the full (normalized) Reynolds and Maxwell stress tensors are

$$
\frac{\langle u_i u_j \rangle}{\langle u^2 \rangle} = \begin{pmatrix} 0.25 & 0.09 & 0.00 \\ 0.09 & 0.62 & -0.00 \\ 0.00 & -0.00 & 0.13 \end{pmatrix},
$$
$$
\frac{\langle B_i B_j \rangle}{\langle B^2 \rangle} = \begin{pmatrix} 0.03 & -0.09 & 0.00 \\ -0.09 & 0.91 & -0.00 \\ 0.00 & -0.00 & 0.06 \end{pmatrix}.
$$
(24)

Here we used averages over the entire box, except for the (x, z) and (y, z) components where we averaged separately over the upper and lower disk planes (results are given for the upper disk plane). We also compared with averages taken only over the outer layers near the surface and found that the results are not very different. Both the velocity and magnetic field correlation matrices are dominated by the (y, y)-component.

There are new and powerful observational techniques being developed that, in the near future, will allow more detailed comparisons with model predictions. The turbulent velocity field affects the line opacity experienced by the radiation emitted from the disk. Thus, the strength of emission lines and their profiles are a function of the properties of the turbulence in the accretion disk (Horne 1995). These effects are most easily determined by Doppler tomography, for instance differences in thermal and turbulent line broadening will affect the surface brightness of the disk differently for different chemical elements. Also, as the statistical correlations of the different velocity components affect the line profiles and Doppler maps in different ways, detailed information on the statistical properties of the turbulence is in principle obtainable.

The (y, y)-component of the velocity correlation matrix is only observable on the approaching and receding sides of the disk, that is the parts of the disk with the largest Doppler shifts

caused by Keplerian rotation. Accordingly the wings and peaks in the emission line profile will be selectively enhanced due to the decreased line opacity caused by the turbulence, whereas no amplification occurs at the center of the line, as it is produced on the front and back sides of the disk. However this selective amplification becomes less noticeable due to the contribution from the (x, x)-correlation, which decreases the line opacity on the front and back sides of the disk instead, i.e., the regions that form the center of the line profile. It is especially interesting to note that the (y, z)-component, which is the only component that can cause line asymmetries (Horne 1995), is practically vanishing in our simulation.

4. DISCUSSION

The local process of dynamo-generated turbulence appears to be a viable mechanism for turbulent transport in accretion disks. While we cannot exclude other potentially important mechanisms, such as global instabilities (density and tidal waves), or a local Balbus-Hawley instability driven by the magnetic field originating from the central object, it is quite clear that the process studied in the present paper should operate in any case. Thus, based on our model, we might expect a scenario involving transonic and supersonic turbulence, together with small scale and large scale magnetic fields in superequipartition with the turbulence. Those large-scale magnetic fields possibly exhibit cycles on a time scale of tens of orbits. The turbulence acts essentially as a catalyst that allows the system to extract energy from the shear flow. It is therefore not surprising that magnetic fields (both small and large scale) are generated that exceed the kinetic energy of the turbulence.

There are a variety of conceivable improvements to our model. The most important one includes a more realistic treatment of the equation of state and the radiative transfer. Only then will it be possible to model realistically those regions of the disk that are accessible to observations. If the more realistic models continue to show magnetic cycles, we should expect that such variability could also be identified observationally. Also, there still remains a need for global models (cf. Knobloch 1992; Curry, Pudritz, & Sutherland 1994) to test not only the applicability of the local approximation, but in particular to study global dynamo action and to address issues related to the evolution of the entire disk.

REFERENCES

Abramowicz, M. A., Lanza, A., Spiegel, E. A., & Szuszkiewicz, E. 1992, Nature, 356, 41
Ashurst, W. T., Kerstein, A. R., Kerr, R. M., & Gibson, C. H. 1987, Phys. Fluids, 30, 2343
Balbus, S. A., Gammie, C. F., & Hawley, J. F. 1994, MNRAS, 271, 197
Balbus, S. A., & Hawley, J. F. 1991, ApJ, 376, 214
Batchelor, G. K. 1967, An Introduction to Fluid Dynamics (Cambridge: Cambridge Univ. Press)
Blaes, O. M., & Balbus, S. A. 1994, ApJ, 421, 163
Brandenburg, A., Jennings, R. L., Nordlund, Å., Rieutord, M., Stein, R. F., & Tuominen, I. 1995, Fluid Mech., submitted
Brandenburg, A., Nordlund, Å., Pulkkinen, P., Stein, R. F., & Tuominen, I. 1990, A&A, 232, 277
Brandenburg, A., & Zweibel, E. G. 1994, ApJ, 427, L91
Cabot, W., & Pollack, J. B. 1992, Geophys. Astrophys. Fluid Dyn., 64, 97
Campbell, C. G. 1992, Geophys. Astrophys. Fluid Dyn., 63, 197
Cannizzo, J. K., Shafter, A. W., & Wheeler, J. C. 1988, ApJ, 333, 227
Cattaneo, F., & Hughes, D. H. 1988, J. Fluid Mech., 196, 323
Chandrasekhar, S. 1960, Proc. Nat. Acad. Sci., 46, 253
———. 1961, Hydrodynamic and Hydromagnetic Stability (Oxford: Clarendon), 384
Curry, C., Pudritz, R. E., & Sutherland, P. 1994, ApJ, 434, 206
Dubrulle, B. 1993, Icarus, 106, 59
Dubrulle, B., & Knobloch, E. 1992, A&A, 256, 673
Dubrulle, B., & Zahn, J.-P. 1991, J. Fluid Mech., 231, 561
Elmegreen, B. G. 1979, ApJ, 231, 372
Foglizzo, T., & Tagger, M. 1994, A&A, 287, 297
Frank, J., King, A. R., & Raine, D. J. 1992, Accretion Power in Astrophysics (Cambridge: Cambridge Univ. Press)
Goodman, J., & Xu, G. 1994, ApJ, 432, 213
Hawley, J. F., & Balbus, S. A. 1991, ApJ, 376, 223
———. 1992, ApJ, 400, 595
Hawley, J. F., Gammie, C. F., & Balbus, S. A. 1995, ApJ, 440, 743
Horne, K. 1995, A&A, in press
Hurlburt, N. E., & Toomre, J. 1988, ApJ, 327, 920
Hyman, J. M. 1979, in Adv. in Computational Methods for Partial Differential Equations, Vol. III, ed. R. Vichnevetsky & R. S. Stepleman (Publ. IMACS), 313
Kaisig, M., Tajima, T., & Lovelace, R. V. E. 1992, ApJ, 386, 83
Kerr, R. M. 1987, Phys. Rev. Lett., 59, 783
Kley, W., Papaloizou, J. C. B., & Lin, D. N. C. 1993, ApJ, 416, 679
Knobloch, E. 1992, MNRAS, 255, 25P
Krause, F., & Rädler, K.-H. 1980, Mean-Field Magnetohydrodynamics and Dynamo Theory (Berlin: Akademie, Oxford: Pergamon)

Kumar, S., Coleman, C. S., & Kley, W. 1994, MNRAS, 266, 379
Lele, S. K. 1992, J. Comput, Phys., 103, 16
Mac Low, M.-M., Norman, M. L., Königl, A., & Wardle, M. 1995, ApJ, 442, 726
Miller, M. C., & Lamb, F. K. 1993, ApJ, 413, L43
Moffatt, H. K. 1978, Magnetic Field Generation in Electrically Conducting Fluids (Cambridge: Cambridge Univ. Press)
Morfill, G., Spruit, H., & Levy, E. H. 1993, in Protostars and Planets III, ed. E. H. Levy & J. I. Lunine (Tucson: Univ. of Arizona Press), 939
Nordlund, Å., Brandenburg, A., Jennings, R. L., Rieutord, M., Ruokolainen, J., Stein, R. F., & Tuominen, I. 1992, ApJ, 392, 647
Nordlund, Å., & Stein, R. F. 1990, Comput. Phys. Comm., 59, 119
Orszag, S. A., & Kells, L. C. 1980, J. Fluid Mech., 96, 159
Papaloizou, J. C. B., & Pringle, J. E. 1984, MNRAS, 208, 721
Parker, E. N. 1975, ApJ, 201, 74
———. 1979, Cosmical Magnetic Fields (Oxford: Clarendon)
Pudritz, R. E. 1981, MNRAS, 195, 881
Roberts, R. H., & Stix, M. 1971, NCAR Tech. Note, No. 60
Rogers, M. M. 1991, Phys. Fluids, A, 3, 144
Rogers, M. M., & Moin, P. 1987, J. Fluid Mech., 176, 33
Różyczka, M., & Spruit, H. C. 1993, ApJ, 417, 677
Ryu, D., & Goodman, J. 1992, ApJ, 388, 438
———. 1994, ApJ, 422, 269
Shakura, N. I., & Sunyaev, R. A. 1973, A&A, 24, 337
Steenbeck, M., Krause, F., & Rädler, K.-H. 1966, Z. Naturforsch., 21a, 369
Stepinski, T. F., & Levy, E. H. 1988, ApJ, 331, 416
Stewart, J. M. 1975, A&A, 42, 95
Stone, J. M., & Hawley, J. F. 1995, in preparation
Tout, C. A., & Pringle, J. E. 1992, MNRAS, 259, 604
Torkelsson, U., & Brandenburg, A. 1994, A&A, 283, 677
Velikhov, E. P. 1959, Soviet Phys.—JETP, 36, 1398
Vishniac, E. T. 1993, in The Cosmic Dynamo, ed. F. Krause, K.-H. Rädler, & G. Rüdiger (Dordrecht: Kluwer), 211
Vishniac, E. J., Jin, L., & Diamond, P. 1990, ApJ, 365, 648
Walker, M. A. 1992, ApJ, 385, 642
Wisdom, J., & Tremaine, S. 1988, AJ, 95, 925
Yoshimura, H. 1975, ApJ, 201, 740
Zahn, J.-P., Toomre, J., Spiegel, E. A., & Gough, D. O. 1974, J. Fluid Mech., 64, 319
Zhang, W., Diamond, P. H., & Vishniac, E. T. 1994, ApJ, 420, 705
Zweibel, E. G. 1987, in Interstellar Processes, ed. D. J. Hollenbach & H. A. Thronson, Jr. (Dordrecht: Reidel), 195
Zweibel, E. G., & Kulsrud, R. M. 1975, ApJ, 201, 63